Chapter 1

Introduction

The development of the gas turbine engine has made a profound impact on modern life. In less than 70 years, gas turbine engines have been developed to where they are commonly used for applications on land, at sea and in air. Gas turbines can greatly range in size, producing power output from tens of kilowatts to hundreds of megawatts. The compactness and high power to weight ratio of the engine has enabled it to dominate the field of aircraft propulsion: gas turbines are now used in all but small aircraft which use reciprocating piston engines. In applications for power generation, gas turbines often have startup cycles of minutes, compared with several days required for conventional steam based coal or oil power plants.

It is often said that gas turbine technology is mature. However, gas turbines are being continually improved to meet changing requirements, such as efficiency, noise, weight and emissions. Many of these objectives are strongly dependent on aerodynamics, which not surprisingly, continues to attract a large amount of research attention around the world. Advances in the understanding of this field have lead to many improvements in gas turbine technology.

The performance of gas turbines is heavily dependent on the compression of air prior to combustion. Many early gas turbines, such as the Whittle engine patented in 1930, used centrifugal compression, which was a well proven technology at that time. Although multi-stage axial compressors had the advantage of greater flow rate to frontal area ratio, many early designs suffered from limitations on material strength and durability. Mechanical failures were often catastrophic for both the invention and the inventor. As these problems were gradually overcome and efficiencies increased, axial compressors became more commonly used in gas turbine engines.

This thesis is concerned with the unsteady aerodynamics of axial compressors. Specifically, the focus of the research is on unsteady boundary layer transition on axial compressor blades: a topic of much interest to both industry and research organisations. This research follows a number of related studies at the University of Tasmania, including Walker [175], Solomon [154] and Hughes [83].

The boundary layer development on the surface of compressor blades has a very significant influence on performance. Not surprisingly, a considerable body of research has been devoted to improving understanding of this topic. The flow in axial turbomachinery is inherently unsteady, resulting in complex and unsteady transitional flow behaviour on blade surfaces. It is common for transition to turbulence to occur by different modes at different locations on a blade surface. The flow on the blade surface often has large periodic fluctuations in laminar–turbulent flow. Chapter 2 of this thesis provides a review of the fundamental modes of boundary layer transition and transitional flow phenomena that occurs on the surface of turbomachine blades.

The low-speed research compressor at the University of Tasmania (UTAS) is extensively used in the experimental studies of this thesis. The research compressor is a 1.5-stage machine, containing three blades rows: inlet guide vanes (IGV), rotor and stator. Chapter 3 describes this facility, associated instrumentation and control systems. Chapter 4 introduces the experimental testing program by first discussing several factors important to low-speed testing. Chapter 4 also details several experimental methods used during the investigations of this thesis.

One goal of the current research is to understand how unsteady flow effects are influenced by higher levels of turbulence, such as those found inside an embedded stage of a multi-stage axial compressor. The real engine environment is not well suited for making sensitive flow measurements, such as flow phenomena close to blade surfaces. Instead, testing is often performed in cascade wind tunnels and research compressors. Most of these facilities, including the UTAS research compressor, naturally have a low inlet turbulence level. In the present study, the inlet turbulence was increased to levels typical of an embedded stage by installing a grid upstream from the compressor section.

Chapter 5 describes a study of the influence of turbulence on the unsteady flow field in the axial space between the rotor and stator blade rows. Surveys using a single-element hot-wire probe are made over one blade pitch at mid-span. The measurements are processed to determine temporal variations in ensemble averaged velocity and

turbulence. These results are compared with previous measurements by Hughes [83] made using the low inlet turbulence configuration of the compressor. The study shows how turbulence level influences unsteady flow effects such as IGV wake dispersion and IGV wake – rotor wake interaction, and also the pitchwise variation of velocity and turbulence properties.

Chapter 6 studies how free-stream turbulence and blade row clocking influence the unsteady transitional flow on the surface of a C4 stator blade at mid-span. Measurements from an array of hot-film sensors attached to a stator blade are processed to determine the temporal variation of ensemble average intermittency. These results are compared with similar measurements made at low inlet turbulence by Hughes [83], which showed that blade row clocking has a large influence on stator blade boundary layer development. That study showed aligning the IGV wakes in the stator blade passage resulted in large temporal fluctuations of laminar–turbulent flow on the stator suction surface at near design blade load. Immersing the stator blade row in IGV wake turbulence increased the level of turbulent flow on the suction surface. The present study shows that the latter flow behaviour is very similar to that at high inlet turbulence with the IGV wakes aligned in the stator blade passage. Significant conclusions are made about the influence of free-stream turbulence on blade row clocking and the ability of 1.5-stage axial compressors to simulate an embedded stage in a multi-stage turbomachine.

Axial compressor design has evolved over time. In aviation applications, weight must be kept to a minimum. This has driven compressor design to not only improve efficiency, but also to reduce the number of blades in each row, increasing individual blade loadings. A popular design methodology, known as controlled diffusion (CD), achieves high levels of efficiency by controlling the boundary layer development on blade surfaces. It is common industry practice to use a circular arc leading edge profile in blade design: although not optimal, it may be argued that this provides a balance between a practical geometry for manufacturing and satisfactory aerodynamic performance. The flow rapidly accelerates around the circular arc section and then rapidly decelerates near the blend point of the arc section to the main surface, producing a spike in the surface velocity distribution. In some cases this has been known to cause boundary layer separation, transition and reattachment at the leading edge. It is also common design practice for CD compressor blades to have a region of accelerating flow on the suction surface from the leading edge to peak suction, which

is usually located at 20–40 percent chord. The CD design methodology raises several questions regarding the boundary layer development on blade surfaces. Do circular arc leading edges promote fully turbulent flow on the blade surfaces? Does the region of accelerating flow on the suction surface have a beneficial effect on the boundary layer development? How is boundary layer influenced by unsteady wake passing events? In order to investigate questions such as these, a new stator blade row was specifically designed for testing in the UTAS research compressor, replacing the existing C4 stator blade row. The blade was designed to produce similar outlet flow conditions as the existing C4 stator. The stator surface pressure distribution was designed to be typical of modern high-pressure compressor blading. The blade profile featured a circular arc leading edge. Chapter 3 describes manufacturing of this blade row and subsequent installation into the research compressor.

Chapter 7 investigates the flow through the CD stator blade row. Mid-span surface pressure distributions at are obtained from slow-response pressure measurements. These measurements are compared with numerical predictions using the steady flow, quasi three-dimensional solver, MISES. Both measured and predicted time-mean velocity distributions show large leading edge velocity spikes as anticipated.

Unsteady transitional flow on the surface of a CD stator is studied using an array of surface mounted hot-film sensors at mid-span. Analysis shows that the suction surface boundary layer does not become completely turbulent at the leading edge as predicted by the MISES flow solver. The flow exhibits strong periodicity with large temporal fluctuations in laminar–turbulent flow. Turbulent spots and instability phenomena are examined for convection speed, growth rate and evidence of relaminarisation. In contrast, the flow on the pressure surface becomes completely turbulent at the leading edge and is relatively insensitive to Reynolds number and incidence. The study emphasises the significant influence of the leading edge profile on compressor blade boundary layer development.

Chapter 8 studies the influence of passing rotor wakes on laminar boundary layer stability at the leading edge of both C4 and CD stator blades. The unsteady flow through both the C4 and CD stator blade rows is simulated using the unsteady quasi three-dimensional flow solver, UNSFLO. The unsteady flow simulations are validated by comparing predicted skin friction measurements with ensemble average quasi wall shear stress measurements obtained from surface mounted hot-film sensors. Rotor wake chopping is shown to have a destabilising effect on the suction surface boundary

layer and a stabilising effect on the pressure surface boundary layer.

Examination of raw hot-film data reveals a variety of transitional flow phenomena at the leading edge of both stator blades. Both viscous instability waves and puff type disturbances typical of bypass transition are observed under the rotor wake trajectory. Observations are made regarding the nature and frequency of occurrence of these disturbances. The results point to the leading edge as the principal receptivity site for wake-induced bypass transition occurring on the suction surface of both C4 and CD stator blades. The flow behaviour observed on the pressure surface is more consistent with buffeting of the boundary layer by passing rotor wake turbulence; these observations are more consistent with other studies of the flow on turbine blade surfaces where the relative convection of rotor wake fluid is toward the blade.

A final summary of the most important findings of this thesis and recommendations for future research are presented in Chapter 9.

Supporting Publications

Several components of the work described in this thesis have been published during the course of the project. Studies of the influence of turbulence on wake dispersion and wake–wake interaction effects reported in Chapter 5 were published in Henderson et al. [66]. The investigation of turbulence level and loading on the transitional boundary layer behaviour of a C4 stator described in Chapter 6 was published in Henderson et al. [67]. In addition, the study of transitional flow phenomena occurring at the leading edge of a C4 stator blade, detailed in Chapter 8, was published in Henderson et al. [68].

Chapter 2

Literature Review

2.1 Introduction

The flow in gas turbine engines is highly turbulent and unsteady. The dispersion of turbulent blade wakes across many blade rows results in high levels of free-stream turbulence; and the relative motion between blade rows leads to a range of complex fluid flow phenomena. Transition to turbulence on blade surfaces is unsteady, and may occur by multiple modes at different surface locations. Despite the complex flow behaviour, significant portions of the blade surface boundary layers are often in a laminar or transitional state. Predicting the flow behaviour in these conditions is difficult. The numerical tools used by engine designers need to make approximations where possible in order to achieve an acceptable balance between speed and accuracy. Better understanding of transitional flow phenomena is required to facilitate the improvement of existing models. Experimental data is also required to validate numerical models.

Extensive reviews on the role of laminar–turbulent transition in gas turbine engines were given by Mayle [111] and Walker [177]. Since this time there have been significant further advances in the understanding of transitional flow behaviour. In order to approach this subject in a logical way, this chapter first reviews the basic modes of boundary layer transition. This is followed by a review of common models used to describe the onset of transition and breakdown to turbulent flow (turbulent spot theory). This provides the background necessary for the concluding discussion of transitional flow phenomena in turbomachines.

2.2 The Modes of Transition

Boundary layer transition from laminar to turbulent can occur by substantially different mechanisms. These have been categorised into different 'modes' of transition based on experimental observation. Understanding these modes is important since each mode can result in very different flow behaviour. The following sections review the fundamental modes of transition.

2.2.1 Natural Transition

Natural transition in a boundary layer usually occurs in flows with low turbulence and pressure gradients mild enough to avoid stabilisation or separation. The transition process is *natural* because it occurs without external forcing. The process is characterised by a number of stages that take place over a relatively long streamwise length scale. This has allowed researchers to make detailed studies of the flow behaviour. The following paragraphs describe the main stages of natural transition.

In the first stage, a laminar boundary layer has grown in thickness to the point where small disturbances in the flow may be amplified. These initial disturbances can originate from a range of possible sources, including sound or vorticity [142]; the term *receptivity* is used to describe the boundary layer response. The resulting boundary layer disturbances are amplified at a near linear rate to form two-dimensional *Tollmein–Schlichting* (T–S) waves. The inception and initial growth of these waves is well predicted by linear stability theory (see Section 2.4). Many researchers have studied natural transition processes by artificial forcing of the boundary layer to introduce T–S waves into the flow: for example, the vibrating ribbon technique used by Schubauer and Klebanoff [150]. In these studies the artificially initiated T–S waves grew and behaved very similarly to natural occurring waves.

The second stage of the breakdown process is characterised by a spanwise distortion of the T–S waves. This was observed by Knapp and Roache [96] using smoke visualisation on an ogive nose cylinder (see Fig. 2.1). This three-dimensional distortion continues, resulting in the generation of streamwise vorticity components and the formation of an array of vortex trusses ('hairpin eddies' or 'Λ-vortices').

In the fourth stage of breakdown, further high frequency instability occurs near the head of the vortex loops, and these small-scale disturbances break down to initiate turbulent spots. Westin et al. [186] explains that the mechanism for the non-linear

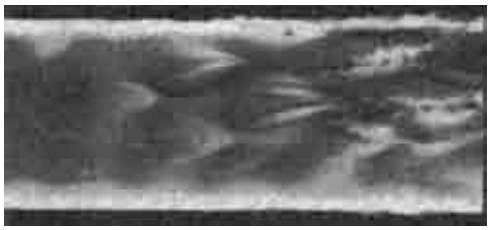

Figure 2.1: Smoke visualisation of vortex trusses (from Knapp and Roache [96])

breakdown is largely dependent on free-stream flow conditions.

Once initiated, turbulent spots grow in size as they travel downstream, eventually merging with other spots to form a continuously turbulent boundary layer. The growth and merging of turbulent spots was observed in the early water table experiments of Emmons [40] and is described in Section 2.5. A schematic diagram of natural transition on a flat plate given by White [188] is shown in Fig. 2.2.

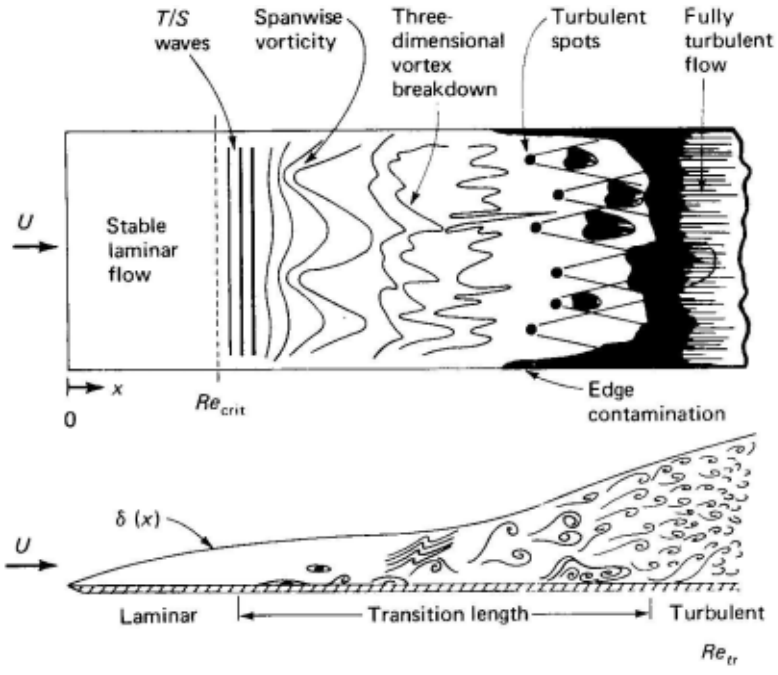

Figure 2.2: Schematic diagram of the natural transition process (from White [188])

Discrete packets of instability waves may develop in unsteady flow. Obremski and Fejer [121] studied transition on a flat plate with a periodically oscillating free-stream velocity. Discrete packets of instability waves resembling T–S waves were observed. Cohen et al. [22] made detailed observations of wave packets artificially generated by a short duration air pulse. Both the initial frequency and growth of the

wave packets agreed well with predictions based on linear stability theory. The wave packets observed in these studies eventually broke down to form turbulent spots.

It has been a long held belief that natural transition, being associated with low turbulence flows, plays no role in transition in highly turbulent flows in multi-stage turbomachines [111]. However, instability waves have been observed to propagate in flows with up to 1.5% turbulence intensity, and may also participate in the non-linear processes leading to the formation of turbulent spots [13]. Hughes and Walker [85] detected instability waves on the surface of a compressor blade using a wavelet analysis technique. Wave packet activity was detected in practically all cases preceding transition to turbulent flow. These studies have shown that instability waves responsible for natural transition may still be involved in transition process on the surface of turbomachinery blades, although the dominant breakdown mechanism may differ depending on flow conditions.

2.2.2 Bypass Transition

Bypass transition occurs in boundary layers subjected to large amplitude external disturbances from the free-stream flow. One of the earliest references was given in a review of transition processes by Morkovin [117], who proposed an alternative mechanism leading to the formation of turbulent spots that bypasses some of the stages of natural transition. The term now encompasses a multitude of mechanisms occurring in highly disturbed flows.

Klebanoff [95] observed low frequency oscillations in hot-wire measurements of a boundary layer subjected to free-stream turbulence. Later studies by other researchers showed that this effect was caused by the slow spanwise motion of elongated streamwise structures (also termed 'streaky structures' or 'breathing modes'): these were named *Klebanoff modes* and are distinctly different from T–S waves observed in natural transition. Blair [9] observed Klebanoff modes in a boundary layer subjected to intense free-stream turbulence. Measurements using a hot-wire probe revealed multiple 'negative spikes' proceeding the formation of turbulent spots. No evidence of T–S waves in the boundary layer prior to breakdown was found in that study.

Studies of turbulent spots and unsteady wake-induced boundary layer transition were made by Zhong et al. [199] and Zhong et al. [198] using a thermochromic liquid crystal flow visualisation technique. Anthony et al. [4] also studied bypass transition using surface heat flux imaging. These studies show that streaky structures are usually

present prior to transition in boundary layers subjected to high levels of free-stream turbulence.

Recent computational studies have provided useful information about the formation and evolution of streaky structures. Jacobs and Durbin [90] used direct numerical simulation (DNS) to investigate bypass transition in a flat plate boundary layer. High levels of free-stream turbulence were simulated by summing the continuous modes of the Orr–Sommerfield equation. The study also showed that the elongated structures resulted from interactions between the boundary layer and turbulent eddies in the free-stream flow. A small percentage of streaks were observed to generate turbulent spots. A visualisation of the simulation is shown in Fig. 2.3.

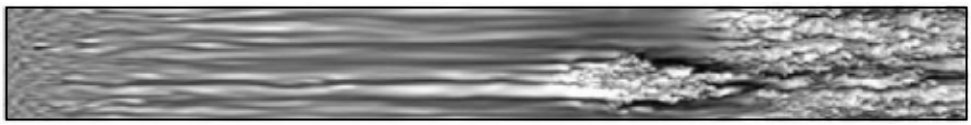

Figure 2.3: Visualisation of DNS solution showing streaks proceeding turbulent breakdown (from Jacobs and Durbin [90])

Numerical simulations by Zaki and Durbin [196] demonstrated that free-stream disturbances can interact with the boundary layer to generate packets of Squire modes, which in certain situations may result in the formation of Klebanoff modes.

Zaki et al. [197] used DNS to study the steady flow through a linear compressor cascade. A free-stream turbulence intensity of 3.2% was prescribed at the inlet of the model domain. The boundary layer on the pressure surface of the blade developed elongated boundary layer perturbation jets (or streaks) that eventually lead to the formation of turbulent spots. Streaks did not form on the forward part of the suction surface. The boundary layer separated further along the surface in the adverse pressure gradient following peak suction. Breakdown to turbulence occurred by Kelvin–Helmholtz billows originating in the outer part of the boundary layer. It is possible that the favourable pressure suppresses the formation of streaks, although surface curvature may also be an influencing factor.

2.2.3 Separated Flow Transition

The persistence of laminar flow at low Reynolds number may lead to separation of a laminar boundary layer in regions of adverse pressure gradient. The detached laminar shear layer is highly unstable and undergoes rapid transition, leading to greater

entrainment of fluid into the shear layer. If the adverse pressure gradient is not too strong, the dividing streamline will turn back toward the surface, resulting in reattachment of the shear layer. The resulting closed region of recirculating flow is commonly referred to as a separation bubble. A schematic diagram of separated flow transition from Mayle [111] is shown in Fig. 2.4, where boundary layer separation, transition onset and completion, and boundary layer reattachment are denoted by x_s, x_t, x_T and x_r respectively.

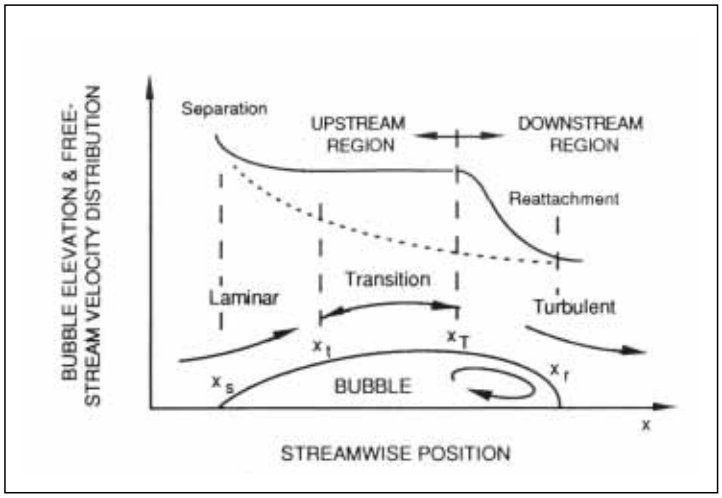

Figure 2.4: Schematic diagram of separated flow transition (from Mayle [111])

Research has shown that separation bubbles are not restricted to purely laminar flows. Hatman and Wang [64] identified three different modes of separated flow transition: transitional separation where the transition process has commenced prior to separation, and short and long separation bubbles, which are classified according to their relative streamwise length scale.

Advances in computational methods and experimental techniques have allowed separated flow transition to be studied in greater detail. A review of current literature shows that breakdown may occur by several mechanisms. Roberts and Yaras [136] used large eddy simulation (LES) to study the behaviour of a separation bubble. Their study showed the development of inviscid Kelvin–Helmholtz (K–H) instability over the rear part of the bubble, which resulted in shedding of large scale eddies. These eddies travelled downstream where they broke down into smaller structures. The power spectrum of velocity fluctuations prior to breakdown revealed high energy fluctuations at frequencies similar to the most unstable T–S frequency predicted from linear stability theory (see Walker [176]). Yang and Voke [195] reached a similar

conclusions in a LES study of a leading edge separation bubble. This type of instability was also identified in a wake-induced roll-up of a separated shear layer on the suction surface of a LP turbine cascade [163, 164], as discussed in Section 2.6.2.

Research has also indicated that breakdown can result from other types of instability. Alam and Sandham [2] studied separated flow transition using DNS and observed the formation of highly three-dimensional hairpin or Λ-vortices. These vortices became highly distorted and broke down into smaller eddies. These observations are consistent with an experimental investigation by Lang et al. [98], who used laser-Doppler anemometry (LDA) and particle image velocimetry (PIV) to study a separation bubble in a water flow. In both of these studies small amplitude T–S waves were artificially introduced into the boundary layer. Lang et al. [98] noted the breakdown was relatively insensitive to the type of instability introduced.

McAuliffe and Yaras [113] performed a coarse DNS of a separation bubble and observed the growth of instability waves downstream from the point of separation. This led to a roll-up of spanwise vorticity and final breakdown by a K–H mechanism. Experimental studies of separation bubbles have also observed instability waves [56, 126]. These studies suggest that multiple modes of instability can exist simultaneously and undergo complex interactions. It is therefore not surprising that the simplified transition models used in aerodynamic design fail to accurately predict separated flow transition.

2.2.4 Relaminarisation

Relaminarisation, also termed 'reverse transition', is the process by which a fully or partially turbulent boundary layer reverts to a state with similar properties to a laminar boundary layer. This process is known to occur in flows with sufficiently strong acceleration. The process is characterised by a thinning of the boundary layer and a reduction in skin friction to levels typical of laminar boundary layers. The most commonly accepted parameter used to indicate relaminarisation is an acceleration parameter given by

$$K = \nu/U^2(dU/dx) \tag{2.1}$$

Wind tunnel studies by Launder [100], Badri Narayanan and Ramjee [7], Patel and Head [128], Jones and Launder [91] and Narasimha and Sreenivasan [119] show that

a fully turbulent equilibrium boundary layer will relaminarise in flows with K equal to or greater than approximately $3.0 - 3.5(10)^{-6}$. This conclusion has been confirmed in more recent studies by Warnack and Fernholz [183, 184], Escudier et al. [41] and Ichimiya et al. [88]. A corollary of this result is that a laminar boundary layer subjected to a sufficiently strong acceleration will remain laminar and not undergo transition to turbulence.

These studies have shown that relaminarisation, like transition, is not an instantaneous process. Experiments where a boundary layer was relaminarised by short and intense acceleration soon reverted back to a turbulent boundary layer (termed 'retransition') following the acceleration [41, 88, 184].

The thickness of the boundary layer decreases as the boundary layer relaminarises. This led some researchers to conclude that relaminarisation will only occur if the momentum thickness Reynolds number is reduced to a sufficiently low level where viscous effects become significant ($Re_\theta \approx 300 - 400$). However, this notion has been disproved by studies showing relaminarisation to occur at higher values of momentum thickness Reynolds numbers ($Re_\theta > 600$) [160, 184]. The most recent studies of relaminarisation have been performed using boundary layers sufficiently thick to avoid the issue of low Reynolds number effects; this does little to clarify what effect low Reynolds number may have on relaminarisation.

The current level of understanding of the physics of relaminarisation is limited. Sreenivasan [160] discusses several possible mechanisms that may contribute to relaminarisation. Some researchers have suggested that the acceleration parameter K may not be the best parameter to predict the onset of relaminarisation [14, 160, 183], especially considering that K is a local variable independent of Reynolds number and flow history. However, the simplicity of the acceleration parameter K makes it convenient to use in many practical applications and it presently remains the most widely accepted criterion for the onset of relaminarisation.

2.3 Predicting the Onset of Transition

Most procedures used for aerodynamic design of turbomachines are customised to favour particular types of analysis. Accurate modelling of transition is essential in obtaining accurate predictions of loss and turning through turbomachinery blade rows [111]. Despite this fact, predicting the onset of transition remains a weak point for transition modelling [178]. The following section describes some common approaches used to predict the onset of transition.

Hall and Gibbings [59] reviewed different approaches used to predict the onset of transition and proposed a new correlation for the momentum thickness Reynolds number at the onset of transition (Re_{θ_t}) in terms of average free-stream turbulence intensity between the leading edge and transition inception (Tu^*). This may be written as

$$Re_{\theta_t} = 190 + \exp\left[6.88 - 1.03(Tu^*)\right] \tag{2.2}$$

where Tu^* is expressed in percent. Abu Ghannam and Shaw [1] revised this correlation to account for the effects of both pressure gradient and turbulence intensity. This may be expressed as

$$Re_{\theta t} = 163 + \exp\left[F(\lambda_\theta) - \frac{\lambda_\theta}{6.91}\right] Tu^* \tag{2.3}$$

where the function F is defined in terms of the pressure gradient parameter λ_θ by

$$F(\lambda_\theta) = \begin{cases} 6.91 + 12.75(\lambda_\theta) + 63.64(\lambda_\theta)^2, & \lambda_\theta \leq 0 \\ 6.91 + 2.48(\lambda_\theta) - 12.27(\lambda_\theta)^2, & \lambda_\theta \geq 0 \end{cases} \tag{2.4}$$

The value of $Re_{\theta_t} = 163$ was based on the critical value of Re_θ predicted by linear stability theory for steady flow over a flat plate with zero pressure gradient. However, this concept is erroneous as fluctuations of the boundary layer profile in response to free-stream unsteadiness may lead to much lower instantaneous values of critical Reynolds number; and critical values of Re_θ predicted by stability theory do not necessary guarantee the sustainability of turbulent flow.

Another popular approach for predicting transition inception in flows with free-stream turbulence is to correlate momentum thickness Reynolds number at transition onset in terms of local free-stream disturbance level. This was done by Hourmouziadis

[79], who proposed the following correlation

$$Re_{\theta t} = 460 Tu^{-0.65} \tag{2.5}$$

Mayle [111] later obtained a similar result based on a slightly different set of data. This may be written as

$$Re_{\theta t} = 400 Tu^{-5/8} \tag{2.6}$$

Numerical flow solvers may determine the onset of transition in a number of ways. Savill [144, 145] provides a concise review of the ability of various numerical methods in modelling transitional flow behaviour. The large number of numerical methods will not be individually discussed here; but they may be broadly classified into three main approaches. In the first approach, transition is modelled as a superposition of laminar and turbulent components. Empirical data is usually required to specify the location and progression of transition. An example of this approach is the algebraic turbulence model of Cebeci and Smith [19].

The second approach uses a turbulence model such as the well known k–ϵ, k–L or k–ω models. Transition is implicitly modelled by the process of diffusion of turbulent energy from the free-stream into the boundary layer. Early studies by Schmidt and Patankar [148, 149] using a k–ϵ model showed that solutions were sensitive to both turbulence model parameters and the inlet turbulence, which is undesirable for use in general applications [161]. Many recent low-Reynolds number turbulence models are achieving encouraging results; however, a fundamental problem with the turbulence model approach is that it does not mirror the exact physics of transition as indicated by more recent DNS studies [144].

The third approach, pioneered by Steelant and Dick [161], involves solving a transport equation for intermittency in addition to the governing flow equations. Recent examples of this method include Menter et al. [114] and Langtry et al. [99], which use an empirically-based correlation for vorticity Reynolds number to determine the transition onset location. The intermittency factor is then directly coupled to productive and destructive terms of the turbulence model. Another method, developed by Suzen and Huang [165], uses separate correlations for predicting the onset of attached and separated flow transition. The intermittency factor is incorporated into

the flow equations by scaling the eddy-viscosity. Methods using the intermittency transport method generally show better agreement with experimental results than methods that use the second approach described above. Despite this, they suffer from the same fundamental problem noted in the second approach.

Advanced numerical methods such as large eddy simulation (LES) and direct numerical simulation (DNS) have gained recent popularity as research tools, but they remain too computationally expensive for most applied applications including industrial design.

The approximate correlations given by Eqns (2.3) and (2.6) are relatively easy to implement in numerical methods. However, as noted by Solomon et al. [158], the level of accuracy obtained is usually insufficient to predict flow phenomena such as separated flow transition. These methods do not account for the influence of turbulent length scale on transition, which is generally accepted, but not well understood [16, 112]. In addition, the strong pressure gradients found in turbomachinery flows can lead to amplification of turbulence near the leading edge of blades [71], and an anisotropic variation of turbulence properties [159]. Voke et al. [174] discuss an LES study of transition following a leading edge separation bubble. The anisotropy of the inlet turbulence was altered by specifying fluctuations of u', v' and z' in turn. The wall-normal component of turbulence v' was found to be most influential in initiating the transition process.

2.4 Linear Stability Theory

The onset of the natural transition process in a boundary layer may be predicted by theoretical consideration of the governing flow equations. This approach is known as *linear stability theory* and it continues to provide useful information about the physical processes of transition. The following paragraphs describe the basic theory and how it relates to turbomachinery flows. A more detailed description of linear stability theory can be found in Schlichting [147].

Schlichting [146] and Tollmien [170] applied small disturbance theory to the Navier–Stokes equations for a laminar wall-bounded flow. The disturbances were assumed to be two-dimensional, and periodic in both space and time as expressed by the stream

function

$$\psi(x, y, t) = \phi(y)e^{i(\alpha x - \beta t)} \tag{2.7}$$

with the complex variables $\beta = \beta_r + i\beta_i$ and $c = \beta/\alpha = c_r + ic_i$. β_r represents the circular frequency of the oscillation, c_r is the phase velocity of the wave, and β_i and c_i are amplification factors. The streamwise wavelength of the oscillation is $\lambda = 2\pi/\alpha$. $\phi(y)$ represents the variation of disturbance amplitude across the boundary layer.

The Navier–Stokes equations were simplified by assuming two-dimensional flow parallel to the wall and omitting higher order terms. The disturbance equation Eq. (2.7) was then substituted into the simplified Navier–Stokes equations. Considerable manipulation yields a single fourth-order differential equation known as the Orr–Sommerfield equation. This may may be written as

$$(U - c)\left(\phi'' - \alpha^2\phi\right) - U''\phi = -\frac{i}{\alpha R}\left[\phi'''' - 2\alpha^2\phi'' + \alpha^4\phi\right] \tag{2.8}$$

Equation (2.8) describes the complex amplitude of a disturbance propagating through the boundary layer. Appropriate choice of boundary conditions makes Eq. (2.8) an eigenvalue problem. The eigen-solutions are commonly presented as a stability diagram showing lines of constant amplification rate on a plot of dimensionless disturbance wave number or frequency against boundary layer Reynolds number (e.g. Fig. 2.5). Disturbances that lie inside the contour for $c_i > 0$ are amplified, and those that fall outside are damped. The zero amplification line is referred to as the neutral stability curve; it defines the critical boundary layer Reynolds number below which disturbances of all frequencies are damped. The streamwise position where the boundary layer Reynolds number first becomes equal to the local critical value is termed the neutral stability point. Disturbances occurring upstream from this point are dampened and disturbances occurring downstream are amplified. The critical boundary layer Reynolds number is often expressed in terms of pressure gradient parameter (λ_θ), or alternatively boundary layer shape factor (H) by assuming similarity between H and λ_θ (see Rosenhead [140]).

The distance between the neutral stability point and the point of breakdown depends on the rate at which disturbances are amplified. Experimental measurements of T–S waves show that the amplification is for the most part linear, becoming non-

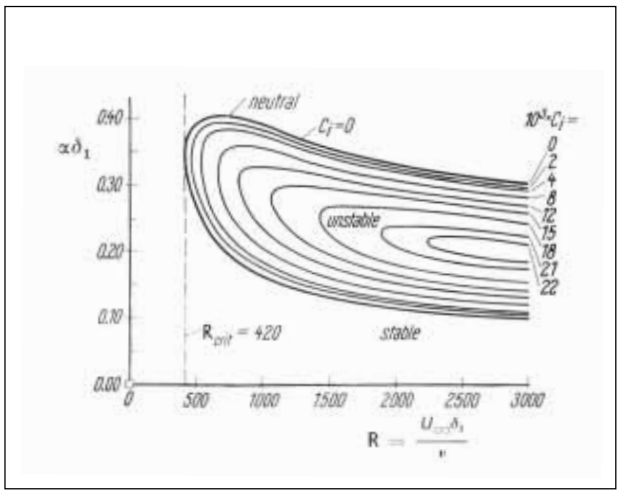

Figure 2.5: Disturbance amplification curves for the boundary layer on a flat plate at zero incidence. δ_1 denotes boundary layer displacement thickness (from Schlichting [147]).

linear shortly before breakdown. Some researchers have used linear stability theory to estimate the spatial distance between the neutral stability point and the point of turbulent breakdown. One such method was the 'e^n' method pioneered by Smith and Gamberoni [152] and van Ingen [172]. This method was based on earlier proposition by Liepmann [103], who suggested turbulent breakdown occurs where the ratio of shear stress associated with instability waves to viscous shear stress exceeds some critical value. In the method developed by Smith and Gamberoni [152] and van Ingen [172], an amplification ratio n was calculated by estimating the most unstable T–S wave frequency predicted by linear stability theory. Turbulent breakdown was assumed to begin when disturbances had been amplified by a factor of $e^{n_{cr}}$. Smith and Gamberoni [152] studied experimental measurements of transition in low turbulence flows, and suggested that $n_{cr} \approx 9$.

The numerical scheme developed by Gleyzes et al. [51] and Drela and Giles [36] used boundary layer similarity to estimate the local amplification ratio in terms of local boundary layer variables. The onset of transition is determined by integrating the amplification ratio in the streamwise direction, starting from the neutral stability point, until a critical value of the amplification ratio n_{cr} is reached.

Mack [109] suggested that the amplification ratio required for turbulent breakdown should reduce with increasing free-stream turbulence and proposed a correlation to describe the relationship. This correlation, as later modified by Drela and Giles [36]

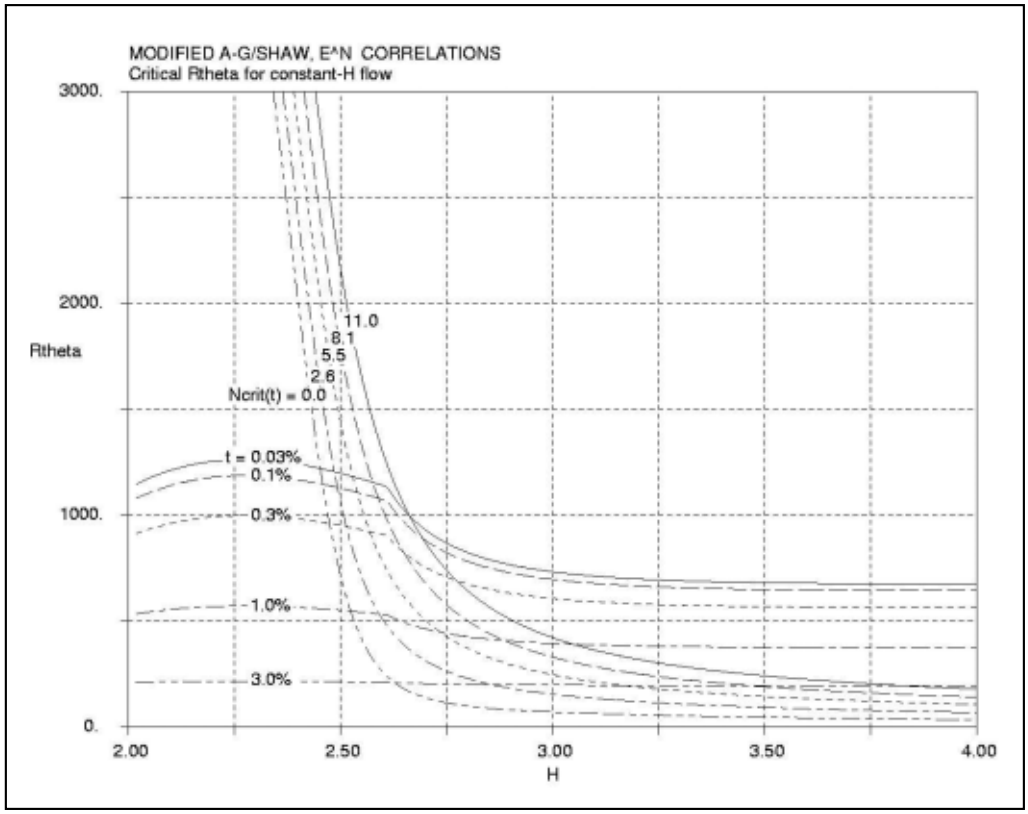

Figure 2.6: Comparison of critical Re_θ for turbulent breakdown for both the e^n and Abu Ghannam and Shaw [1] methods (from Drela [35]). Critical amplification ratio, turbulence intensity, and momentum thickness Reynolds number are indicated by $Ncrit$, t and $Rtheta$, respectively.

to accommodate a wider range of permissible turbulence levels, is given by

$$n_{cr} = -8.43 - 2.4 \ln \left[\frac{Tu}{100} \right] \tag{2.9}$$

where Tu, expressed as a percentage, is the local free-stream turbulence level.

Drela and Giles [36] used this approach in the MISES code, a quasi two-dimensional inviscid–viscous design and analysis system for cascade aerofoils. Transition onset was determined using a hybrid method based on the bypass transition correlation Eq. (2.3) and a variable e^n method as outlined above. Figure 2.6 shows the variation of boundary layer Reynolds number Re_θ for turbulent breakdown versus shape factor H for similar laminar flows. This indicates that transition in accelerating flows with low shape factors is more likely to be predicted by the bypass transition correlation. In decelerating or separating flows, a large value of shape factor results in high amplification ratios and transition is more likely to be predicted by the e^n method. This

approach can predict the boundary layer development on the surface of aerofoils with an accuracy sufficient for many types of engineering calculations (e.g. [36, 97]).

2.5 Turbulent Spot Theory

The final stage in the transition to turbulence of a boundary layer is the growth and merging of turbulent spots. Some of the first recorded observations of this were the water table experiments of Emmons [40]. In these experiments the surface reflections from water running down an inclined table showed turbulent spots appearing and growing in size as they travelled downstream. Emmons noted that the spots were approximately arrow shaped, travelled more slowly than the free-stream, and grew in size until finally merging with other spots to form a continuously turbulent flow. A schematic diagram of this process is shown in Fig. 2.7.

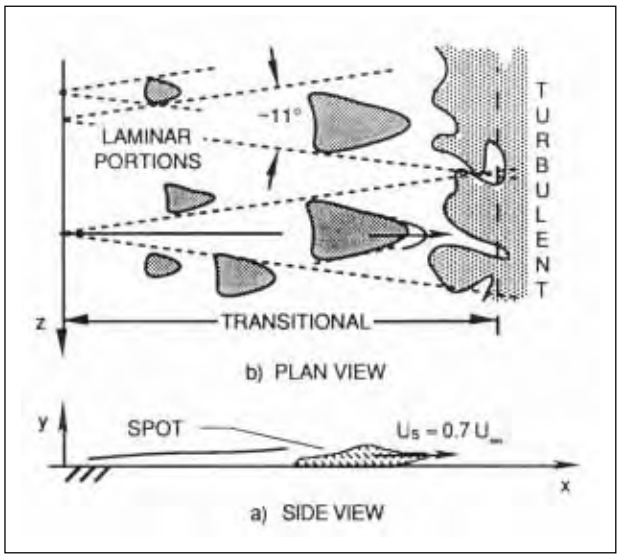

Figure 2.7: Schematic diagram of turbulent spot development (from Paxson and Mayle [129])

These observations enabled Emmons to develop a statistical model for this process, now known as *turbulent spot theory*. Emmons proposed that the probability of point in the boundary layer being turbulent could be calculated by integrating a source rate function over the domain of dependence of the point. The fraction of time the flow at the point is turbulent is referred to as an *intermittency factor* or *transitional intermittency*. Emmons' model of the intermittency factor γ for a point P in the

boundary layer may be expressed as

$$\gamma(P) = 1 - \exp(-\iiint g(P_o)\, dx_o\, dz_o\, dt_o) \tag{2.10}$$

where the function $g(P_o)$ is the source-rate density function representing the turbulent spot production at a point P_o in the domain of dependence of point P as shown in Fig. 2.8.

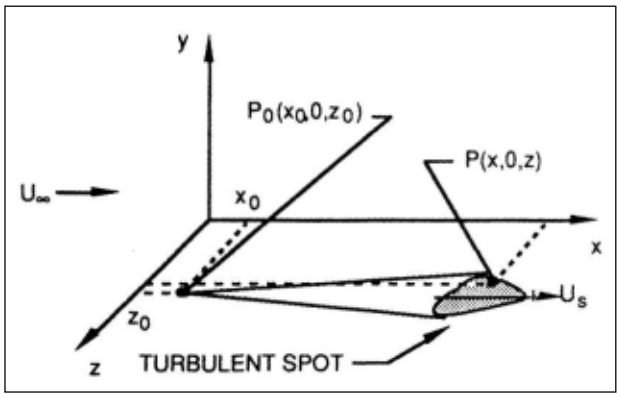

Figure 2.8: The domain of dependence for a turbulent spot (from Mayle [111])

Wind tunnel investigations by Schubauer and Klebanoff [150] gave further detail of turbulent spot behaviour. Turbulent spots in a flat plate boundary layer were periodically generated using electric sparks close to the surface, and hot-wire measurements were made at various streamwise locations. Each spot was followed by a region of calm flow that travelled more slowly than the spot and had a higher wall shear stress than the undisturbed boundary layer. Schubauer and Klebanoff [150] also studied a continuous wedge of turbulence generated from a small sphere placed near the leading edge of a flat plate. They noted that the spanwise spreading angles were similar for both the turbulent wedge and turbulent spots.

Dhawan and Narasimha [28] proposed turbulent spot production rate should be concentrated at a preferred streamwise location near the start of the transition zone. By expressing the source rate function as a Gaussian distribution they found the best agreement with experimental results to occur for a standard deviation approaching zero. In other words, the source rate function could be approximated by a Dirac delta function. This may be expressed as

$$g(P_o) = n\delta(x - x_t) \tag{2.11}$$

where n is the turbulent spot production rate and δ is the Dirac delta function. The transitional intermittency resulting from the concentrated breakdown model of Dhawan and Narasimha [28] may be expressed by

$$\gamma(x) = 1 - \exp\left[-\frac{n\sigma}{U}(x - x_t)^2\right], \qquad x \geq x_t \tag{2.12}$$

where U is the free-stream velocity, x_t is transition onset distance, n is the spot propagation rate and σ is a spot propagation parameter defined by Emmons [40]. The assumption of concentrated breakdown is supported by the experimental observations by Walker and Gostelow [179] and Blair [10].

There have since been several other enhancements made to turbulent spot theory. Chen and Thyson [20] reformulated Eq. (2.12) to allow spot celerities to change with the local free-stream velocity. This improved agreement with measurements in flows with varying pressure gradient, but ignored the more important influence of changing pressure gradient on spot spreading behaviour. Gostelow et al. [54] studied the behaviour of turbulent spots artificially triggered on the surface of a compressor stator and found that the spot spreading angle α and spot propagation parameter were significantly influenced by pressure gradient. Solomon et al. [157] proposed a modification to the Chen and Thyson [20] correlation which accounted for the rapidly changing pressure gradients that are common in turbomachinery flows. This may be expressed as

$$\gamma(x) = 1 - exp\left[-n\int_{x_t}^{x} \frac{\sigma}{tan(\alpha)}\left(\frac{du}{U}\right)\int_{x_t}^{x} tan(\alpha)dx\right] \tag{2.13}$$

The correlations for spot spreading half angle (α) and spot propagation parameter (σ) were later revised by D'Ovidio et al. [34] after more detailed studies of turbulent spots on a flat plate. The final forms are given by

$$\alpha = 4 + 22.14/(0.79 + 2.72\exp(47.63\lambda_\theta)) \tag{2.14}$$

$$\sigma = 0.03 + 0.37/(0.48 + 3.0\exp(52.9\lambda_\theta)) \tag{2.15}$$

where λ_θ is the Pohlhausen pressure gradient parameter for laminar boundary layers.

Although turbulent spot theory was developed from observations of natural transition, various research supports a unified approach which is independent of the mode of transition. Dhawan and Narasimha [28] proposed a dimensionless parameter for

describing turbulent spot production rate, which may be written as

$$N = n\sigma\theta_t^3/\nu \tag{2.16}$$

Narashimha et al. [118] reviewed experimental measurements of transition in low turbulence flows ($Tu > 0.1\%$). Noting N remained approximately constant, Narashimha et al. [118] proposed $N = 0.7(10)^3$. Some time later, Gostelow et al. [53] proposed a correlation for N in terms of free-stream turbulence intensity.

Roberts and Yaras [137] reviewed existing experimental data for both attached and separated transition, and correlated the dimensionless spot production parameter (N) against boundary layer shape factor at transition onset (H_t). The correlation was found to give good agreement with experimental data from both attached and separated flow transition. It may be written as

$$\log_{10}(N) = \frac{0.55H_t - 2.2}{1 - 0.63H_t + 0.14H_t^2} \qquad 1.6 \leq H_t \leq 8.5 \tag{2.17}$$

The shape factor H may be related to pressure gradient parameter λ_θ using similarity solutions of the boundary layer.

Turbulent spot theory has also been successfully applied to predict unsteady transitional flow. Hodson and Schulte [77] developed a predictive technique called the prescribed unsteady intermittency method (PUIM). This method predicts the unsteady intermittency factor $\gamma(x,t)$ based on data supplied by a flow solver. This has since been coupled to a unsteady Reynolds-averaged Navier–Stokes solver by Vilmin et al. [173] and successfully used to predict the unsteady state of boundary layer on a turbine blade [39].

2.6 Transitional Flow in Turbomachinery

The previous sections have reviewed the basic modes of transition from a general viewpoint and described some common approaches used to predict the onset of transition and model the boundary layer transition zone. This section reviews transitional flow phenomena occurring on the surface of axial turbomachine blades.

2.6.1 Periodic Unsteady Transition

The unsteadiness experienced by an embedded blade row in a multi-stage axial turbomachine is partially due to moving pressure fields arising from the relative motion of adjacent upstream and downstream rows. Unsteady effects of this nature propagate both upstream and downstream at sonic speeds relative to the local flow velocity. Machines operating at high-speeds may also develop compressible shock waves (finite discontinuities) travelling at supersonic relative velocities.

Another source of unsteadiness is caused by the dispersion of turbulent wakes from blade rows further upstream. Wakes from one blade row are chopped and rotated in passing through the row immediately downstream. The periodic passing of wakes over each blade surface causes *periodic unsteady transition* in the boundary layers. This has been investigated in numerous studies, most notably Halstead et al. [60–63]. In that comprehensive study, detailed measurements from surface mounted hot-film sensors were made in both a low-speed multi-stage compressor and turbine. Figure 2.9 shows a generalised diagram of the morphology of transition behaviour observed on the compressor stator suction surface at the baseline load case. The passage of an upstream rotor wake over the surface initiates a patch of turbulence that travels along the surface — termed a wake-induced transitional strip (denoted by area B). This

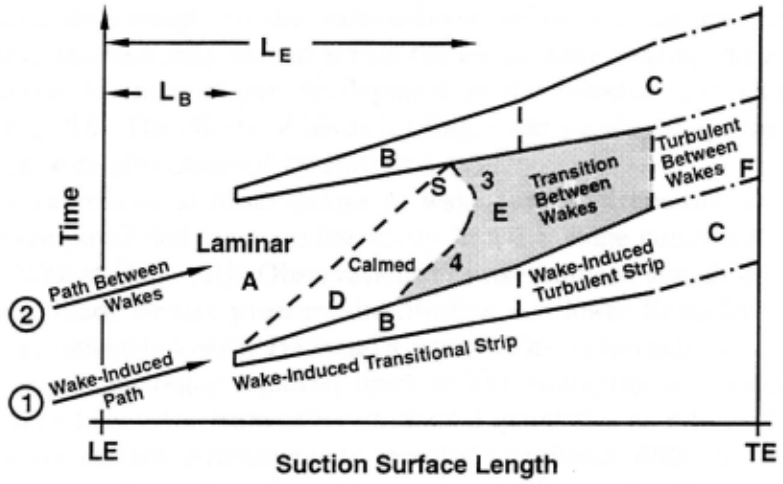

Figure 2.9: Schematic showing the morphology of periodic unsteady transition on a compressor suction surface (from Halstead et al. [61])

strip of turbulence travels more slowly than the free-stream velocity and grows in accordance with the local flow conditions [34]. The strip eventually becomes fully

turbulent (C). A region of calmed flow following the strip (D) actively suppresses separation between wake-induced transitional strips with transitional flow occurring downstream at (E) and fully turbulent flow at (F).

Transition occurring between wake-induced transitional strips is strongly influenced by rotor wake frequency. A low rotor wake frequency may result in the calming effect wearing off prior to the arrival of the next transitional strip. Halstead et al. [63] investigated this by removing a blade from the upstream rotor disk. Measurements from surface mounted hot-film sensors revealed that once the calmed zone had passed the flow between the wakes, the laminar boundary layer separated and reattached as a turbulent layer upstream from the transition location resulting from calmed flow. Similar observations were made by Solomon [154] in an independent study of the flow on an outlet stator blade in the 1.5-stage low-speed research compressor used for the present investigation.

Numerous studies of periodic unsteady transition have been made in cascades and wind tunnels where the test environment can be more easily controlled and larger geometric scales facilitate more detailed observations (Dong and Cumpsty [29, 30], Pfeil et al. [130], Schulte and Hodson [151], Orth [127], Wu and Durbin [193]).

Despite its complexity, periodic unsteady transition can have useful aerodynamic effects. Studies on a flat plate by Thomas and Gostelow [168] showed that the calming effect following a wake-induced transitional strip may persevere in a following turbulent boundary layer. Measurements with a very high frequency of incoming wakes showed that the calming decreased turbulence production within the next turbulent strip.

Schulte and Hodson [151] studied wake-induced transition in a turbine cascade, and found wake passing frequency to be the main factor influencing blade profile losses. The study showed that wake-induced turbulent strips were responsible for suppressing a large separation bubble on the suction side. The calmed region following the strips has greater resistance to separation than a laminar boundary layer under steady flow conditions. The resulting benefit was found to outweigh additional losses associated with the turbulent strips. This discovery has profound implications for the operation of axial turbine blading at low Reynolds numbers and has led to the recent development of modern high-lift and ultra-high-lift blade sections with significant performance benefits [75, 82].

2.6.2 Wake Jet Effect

A blade wake is characterised by high levels of turbulence and a lower velocity than in the free-stream. Meyer [115] noted that the velocity defect of a wake causes a relative convection of wake fluid within the wake. The has been termed a 'negative jet' or 'wake jet' and causes wake fluid to be pushed onto one side and removed from the opposite side of the passage in a downstream blade row (see Fig. 2.10).

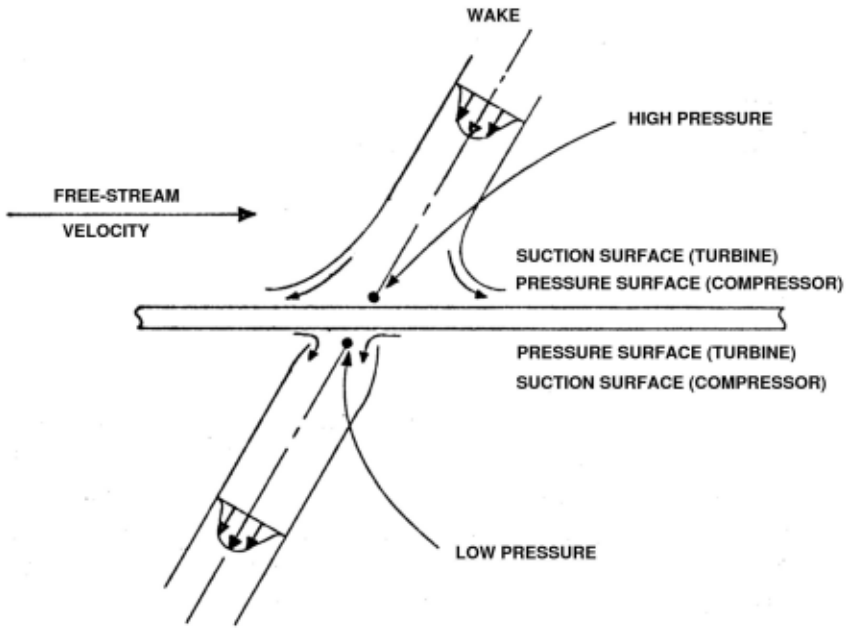

Figure 2.10: Interaction between a convecting wake and flat plate (adapted from Hodson [73] after Meyer [115])

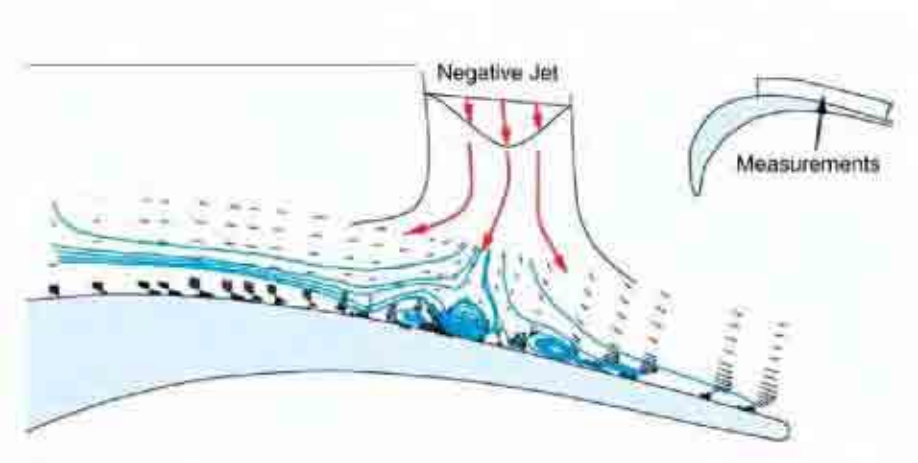

Figure 2.11: Vectors and streamlines showing the interaction between a negative jet and a suction side boundary layer on a LP turbine blade (from Hodson and Howell [75])

In turbines, the negative jet convects wake fluid toward the suction side of a blade. Stieger and co-workers [162–164] studied this interaction in an LP turbine blade cascade. Measurements using laser-Doppler anemometry showed that the interaction between the wake and the separation bubble caused the separated shear layer to roll up into a series of small vortices as depicted in Fig. 2.11. This interaction is characteristic of an inviscid K–H instability. In this case the flow was not perturbed by wake-induced transitional strips since transition had not occurred upstream from separation. A similar conclusion was reached by Sarkar and Voke [143] in a LES study of a wake – separation bubble interaction on the suction surface of a turbine blade.

Michelassi et al. [116] performed an LES computation of a wake-perturbed flow through a linear turbine cascade. The study showed that the wake interacted with the pressure surface boundary layer, generating streamwise vorticity in the form of elongated counter rotating vortex pairs. Michelassi et al. [116] claimed these were not Görtler vortices, but rather structures resulting from the vorticity of the incoming wakes.

There have been few studies on the influence of the negative jet on compressor blade boundary layers. Here the negative jet acts in the opposite sense as in turbine blading, convecting wake fluid toward the pressure surface and away from the suction surface.

2.6.3 Separation Bubbles

Separation bubbles often form on turbine and compressor blades surfaces where a laminar boundary layer is exposed to an adverse pressure gradient. It is common for bubbles to form close to the leading edge on either blade surface, especially at high incidence; they may also occur around mid-chord on the suction side in the adverse pressure gradient following peak suction. As noted in Section 2.2.3, separation bubbles have been traditionally classified as short or long types. Short bubbles have a small and localised effect on the aerofoil surface pressure distribution, whereas large bubbles interact with the exterior flow resulting in a significant reduction in lift and turning. Gaster [48] made comprehensive studies of separation bubble behaviour on isolated aerofoils. Special attention was given to separation bubble 'bursting' phenomenon, where a short separation bubble abruptly changes size to a long bubble, resulting in a sudden loss of lift. Horton [78] later proposed a semi-empirical model for describing separation bubble behaviour. Roberts [138] modified this to develop a predictive

theory describing the growth and bursting of laminar separation bubbles on aerofoil sections.

Leading edge separation bubbles are common in blade profiles with circular arc leading edges. The discontinuity in curvature at the blend point of the circular arc results in rapid deceleration that often produces a separation bubble. Deutsch and Zierke [25–27, 200] performed extensive cascade testing on a double circular arc compressor profile with a circular arc leading edge. Measured boundary layer profiles showed that transition was triggered at some incidence cases by a leading edge separation bubble that was too small to measure. Hobson and Shreeve [70] conducted a similar study on a CD compressor cascade and also found a leading edge bubble to promote early transition on the suction surface. Later compressor cascade studies by Hobson et al. [71] showed that the distortion of free-stream flow near blade leading edges can result in a significant amplification of free-stream turbulence, which will most likely influence the behaviour of leading edge separation bubbles. Another possible cause of turbulence close to the leading edge is the rapid distortion of free-stream eddies as described in studies by Britter et al. [17] and Hunt and Carruthers [87]. These studies clearly show that leading edge separation bubbles can influence the boundary layer development over the entire surface, and thus overall aerodynamic performance.

Leading edge separation bubbles are not restricted to blade profiles with circular arc leading edges. Walraevens and Cumpsty [182] and Liu et al. [105] found that blade profiles designed with elliptical leading edges are less likely to have bubbles at design incidence, but will still develop them at off-design conditions.

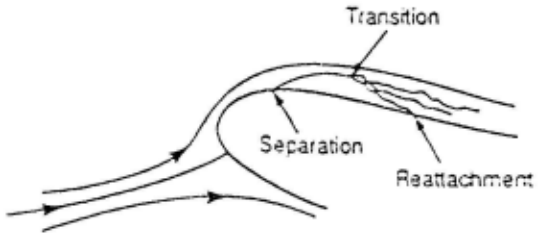

Figure 2.12: Schematic showing leading edge separation bubble (from Tain and Cumpsty [167])

There have been many studies of the interaction between turbulent wakes and mid-chord separation bubbles. Dong and Cumpsty [29, 30] observed this interaction

in a compressor cascade. They found that the separation bubble was periodically suppressed by the passing wakes. Gostelow and Thomas [55] made similar observations of the response of a separation bubble to incoming wakes on a flat plate with compressor-like pressure distribution. The incoming wakes caused wake-induced transitional strips that grew in size as they travelled long the plate. The calmed region following the strips temporarily delayed reformation of the separation bubble after the turbulent strip had passed.

Lou and Hourmouziadis [108] attempted to isolate the effects of wake-jet velocity and turbulence in the wake by installing a rotating flap downstream of a flat plate with compressor-like loading. The unsteady flow did not cause the point of separation to move, but the bubble size fluctuated by approximately 10% of its length in steady flow. However, the velocity fluctuations imposed by the pressure fluctuations in these tests were not representative of those resulting from convective wake disturbances.

The present understanding of the influence of separation bubbles on boundary layer development on axial turbine and compressor blades is still rather limited. This is particularly true of leading edge bubbles, which are difficult to study due to their relatively small size. The situation is further complicated by factors such as geometry, flow incidence, free-stream turbulence, unsteadiness and pressure gradient.

2.7 Conclusions

This chapter has reviewed the fundamental modes of boundary layer transition and transitional flow occurring on axial turbomachine blades. Development in the understanding of boundary layer transition have generally been impeded by the complexity of the flow physics involved. This is particularly true of turbomachinery flow, where blade–blade and blade–wake interactions, together with high free-stream turbulence levels add further complications. Recent advances in computational and experimental methods are now allowing transitional flow to be studied in greater detail than ever before. However, there is still scope for further improvements to be made in the understanding of transitional flow phenomena, in order to develop better design tools for aeroengine blading.

Chapter 3

Experimental Facilities

3.1 Background

In the 1950s a large amount of research activity around the world resulted in the rapid development of gas turbine technology. It was recognised that compressor performance had a strong influence on the overall efficiency of gas turbine engines. A joint research project was commenced between Aeronautical Research Laboratories (ARL) in Melbourne and the University of Tasmania, with a long term goal of developing more efficient compressor blades. Several blade profiles were designed using a technique developed by Lighthill [104], which allowed a blade profile to be analytically defined based on a partially prescribed velocity distribution. Three of these profiles were tested in a low-speed two-dimensional research cascade and their performance compared with British C4 blading. The most promising profile was tested in a high-speed cascade wind tunnel. Blight and Howard [11] reported most sections performed poorly due to a large flow separation on the blade suction side; lack of understanding of boundary layer behaviour meant that the surface velocity distributions were largely specified by trial and error. Lighthill's technique did not account for viscous flow effects such as the boundary layers on a blade surface.

The final stage of the project was the design and construction of a low-speed research compressor. The compressor was designed to achieve free vortex flow at design point operation and is referred to as the 'Vortex Wind Tunnel' in many early publications. The research compressor was manufactured at ARL, Melbourne and transported to the University of Tasmania in 1954. A temporary building was built to accommodate the tunnel during commissioning. The initial measurements were made

using sand cast blades as detailed in a report by Wright and Szomanski [192]. Not long after commissioning, the compressor was relocated to the aerodynamics laboratory at the School of Engineering. Oliver [122] made detailed measurements of the compressor performance with both machined and sand cast blading. In the years that followed, the research compressor was used in many research projects to study unsteady flow phenomena and boundary layer transition on the surface of compressor blades.

This chapter provides details on the research compressor, associated instrumentation and control systems. Additional information, including details of recent equipment upgrades and modifications, is given in Solomon [154] and Hughes [83].

Figure 3.1: UTAS research compressor with the compressor section open showing the rotor and stator blade rows

3.2 Research Compressor Description

The research compressor consists of an axial compressor embedded in an open loop wind tunnel. The tunnel is constructed out of a series of wooden and aluminium sections fastened together with bolts. Most of the internal surfaces are made of plywood with the exception of the working section, which is made from cast aluminium. The wind tunnel is rigidly supported by a steel frame.

Air enters the tunnel radially through a cylindrical inlet 2.13 m in diameter and 0.61 m wide. A wire screen was added across the inlet during the commissioning to improve flow non-uniformity caused by the close proximity of the floor to the lower side of the intake (see Wright and Szomanski [192]). The flow accelerates through a 6.25:1 contraction where it turns through 90° to the axial direction. The test section housing the compressor follows a short distance downstream from the contraction. The test section hub and casing walls have constant diameters of 0.686 m and 1.143 m respectively, giving a hub/tip ratio of 0.6. Details of the compressor test section and blade row configurations are presented in Section 3.3.

The inlet contraction of the tunnel is mounted on a movable frame rolling on fixed tracks which allow the annular rings of the test section to be separated at various locations. Figure 3.1 shows the research compressor open at the stator blade row, exposing both the rotor and stator blade rows. The flow leaves the test section and passes through a conical diffuser approximately 4.5 m long with an included angle of 7°. The hub diameter is constant throughout the test section and diffuser. The flow discharges into the laboratory though a cylindrical throttle which may be automatically controlled to achieve a desired compressor loading. A schematic diagram showing a mid-plane section of the tunnel is shown in Fig. 3.2.

Instruments are inserted radially into the test section through an axial slot in the casing wall. A traversing probe support attached to the wind tunnel frame allows accurate positioning of probes in both axial and radial directions. A telescope mounted above the probe support allows probes inside the compressor to be viewed though a small window in the shell piece.

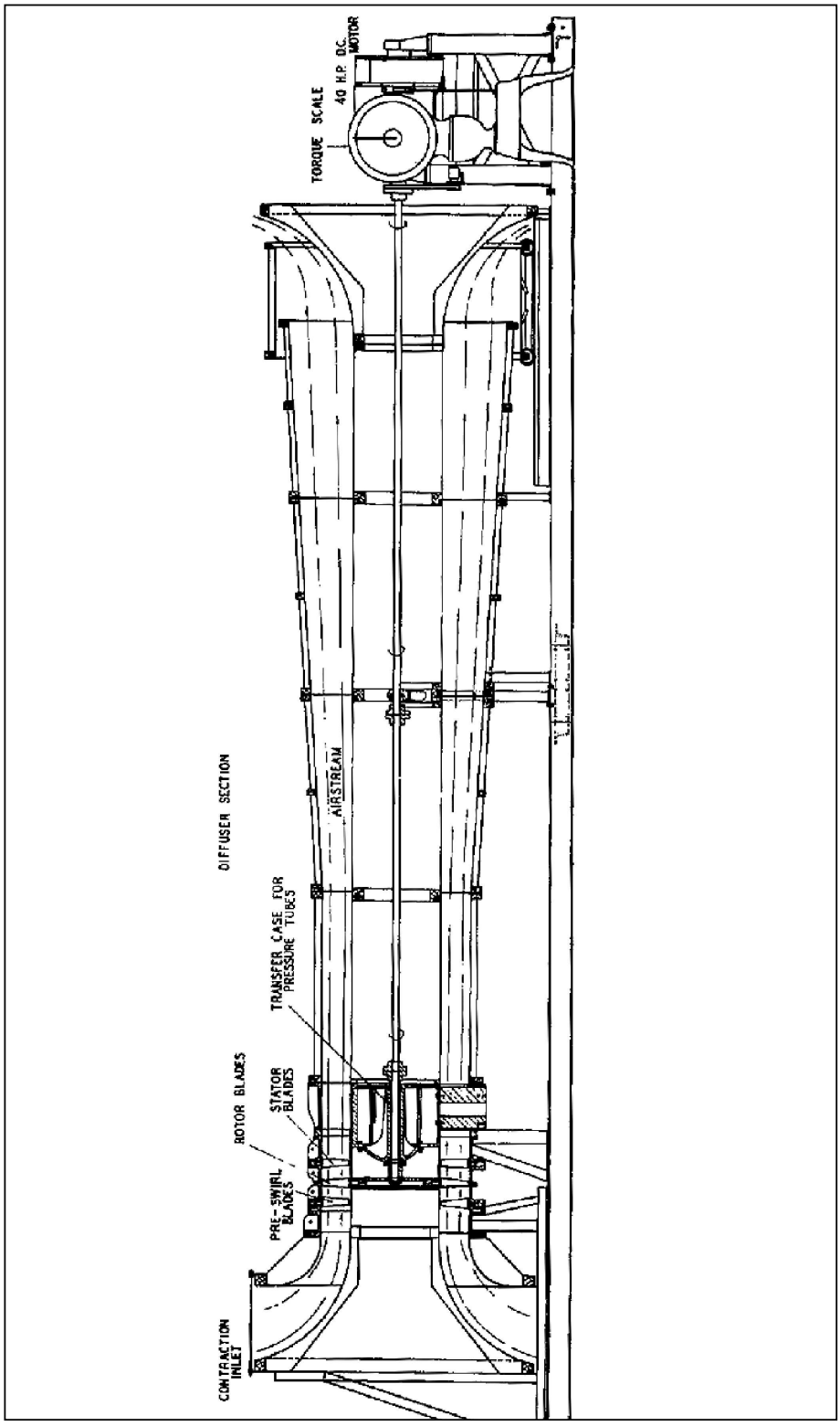

Figure 3.2: Schematic diagram of the research compressor (adapted from Oliver [122])

3.3 Compressor Detail

The compressor is a 1.5-stage machine containing three blade rows: inlet guide vane (IGV), rotor and stator. The IGV and stator blade rows are held in movable rings which allow circumferential traversing over two blade pitches of the original C4 blading. The position of each blade row is controlled by a stepper motor mounted on the outside of the tunnel. This arrangement has the advantage of allowing both IGV and stator blade rows to be circumferentially traversed relative to a fixed probe position, which also allows clocking studies. The position of each blade row at mid-span height is indicated on a vernier scale attached to the compressor shell pieces. This allows the blade rows to be positioned with an accuracy better than ± 1.0 mm at mid-span height. The stepper motor drives may be manually operated or automatically controlled by computer.

Two significant modifications were made to the compressor during previous investigations. The first occurred during reassembly of the rotor blade row during the studies of Solomon [154]. An error was made during setting of the rotor blades which effectively resulted in a 2° increase in rotor blade stagger angle. As noted by Solomon [154], this will cause a slight departure from 50% reaction and free vortex flow at design point operation and also slightly increase the flow coefficient required to stall the compressor. However, this was not considered to significantly influence the mid-span flow behaviour at a given flow angle. The rotor stagger angle was not adjusted in the present study so that direct comparisons could be made with measurements from Solomon [154] and Hughes [83]. Solomon [154] also detailed a correction to allow comparison with measurements taken before the re-stagger.

The other modification was a change in rotor–stator axial spacing made during studies by Hughes [83]. By changing the order of the annular shell pieces in the working section, the axial spacing was reduced from 80.9 mm (106%c) to 31.0 mm (41%c). These configurations were named the long axial gap (LAG) and short axial gap (SAG) respectively. The experimental investigations in the present study used the SAG configuration since it is more typical of axial spacings used in practical machines.

The measurements described in Chapters 5 and 6 were made using the compressor configuration described above. The particular detail of the C4 compressor blading is presented in Section 3.3.1. During the course of the investigation, the C4 stator blade row was replaced with a new stator blade row designed by Hughes [84] in collaboration

with Rolls-Royce plc. This blade row was designed with features typical of modern controlled diffusion (CD) blading while allowing investigation of several issues relating to the shape of the leading edge (Chapter 7). The manufacturing of this blade row and installation in the research compressor is described in Section 3.3.2.

Figure 3.3: The research compressor showing original C4 rotor and stator blade rows (left) and the CD stator blade row with rotor disk removed (right)

3.3.1 C4 Compressor Blading

All blading used in the original configuration of the research compressor were of British C4 section. Each stationary blade row contained 38 blades and the rotor contained 37, giving mid-span space/chord ratios of 0.99 and 1.02 respectively. All blades were designed with a constant chord length of $c = 76.2$ mm and an aspect ratio of 3.0. Hughes [83] measured the chord lengths of 8 blades from each row, reporting the variation to be less than ± 0.2 mm. The blades profiles were stacked about a radial axis to achieve free vortex flow and 50% reaction at mid-span height at design point operation. The maximum profile thickness of 10% chord occurred at a distance of 30% chord from the leading edge. The thickness of the profile may be expressed as a

percentage of chord length by

$$\pm y = \begin{cases} 1.55\sqrt{x} - 0.0656x - 0.00253x^2 + 0.0000281x^3, & x \leq 30\% \\ 3.87 + 0.0787x - 0.00147x^2 + 0.00000345x^3, & x \geq 30\% \end{cases} \tag{3.1}$$

where the coefficients were extrapolated by Oliver [123] from data provided by Howell [81]. The blade profiles were cambered along a circular arc and the small gap at the trailing edge was closed with a circular arc with a radius of 0.58% chord. Figure 3.4 shows a radial view of the stator blade profiles at hub, mid-span and casing.

All C4 blades were machined out of aluminium with the exception of several rotor blades that developed cracks near the blade root. These were replaced with sand cast aluminium blades used in the previous studies of Oliver [122]. All detailed unsteady flow studies involved wakes from machined blades only. Table 3.1 shows the blade angles for the three blade rows. The leading and trailing edge radii for the CD stator are also shown.

3.3.2 CD Stator Blade Row

The CD stator was designed with a constant chord length of 152.4 mm, which is exactly twice the chord length of the C4 stator blades. The use of a longer chord had the advantage of increasing the range of test Reynolds numbers as discussed in Chapter 4. The number of blades were correspondingly reduced to 19, which is exactly half the number of blades contained in the C4 IGV and stator blade rows. This ensured that each stator blade would experience the same pitchwise flow field for a given circumferential alignment between the IGV and stator blade rows.

The CD stator blade profile varies from hub to tip as shown in Fig. 3.4. The blade row was designed to reproduce the outlet flow generated by the C4 stator blade row [84]. The blade was designed using a Rolls-Royce proprietary through-flow program in conjunction with the quasi three-dimensional MISES flow solver of Drela and Giles [36]. Three-dimensional design was not applied to improve the flow quality near endwall regions since the present study is primarily concerned with the flow behaviour at mid-span height.

		Hub	Mid	Casing
I.G.V.	θ	34.4°	27.8°	24.3°
	β_1	0.0°	0.0°	0.0°
	β_2	34.4°	27.8°	24.3°
	ξ	17.2°	13.9°	12.6°
Rotor	θ	52.5°	31.1°	19.1°
	β_1	28.5°	43.0°	49.7°
	β_2	-24.0°	11.9°	30.6°
	ξ	2.2°	27.5°	40.2°
C4 Stator	θ	32.9 (33.5)°	31.1 (35.8)°	29.4 (38.7)°
(CD Stator)	β_1	53.7 (59.6)°	45.0 (53.3)°	39.8 (52.2)°
	β_2	20.8 (26.1)°	13.9 (17.5)°	10.4 (13.5)°
	ξ	37.2 (36.8)°	29.5 (28.9)°	25.1 (25.8)°
	R_{le}	(2.5 mm)	(2.9 mm)	(2.2 mm)
	R_{te}	(2.5 mm)	(2.4 mm)	(1.9 mm)

Table 3.1: Compressor blade details for studies of Solomon [154], Hughes [83], and present investigation

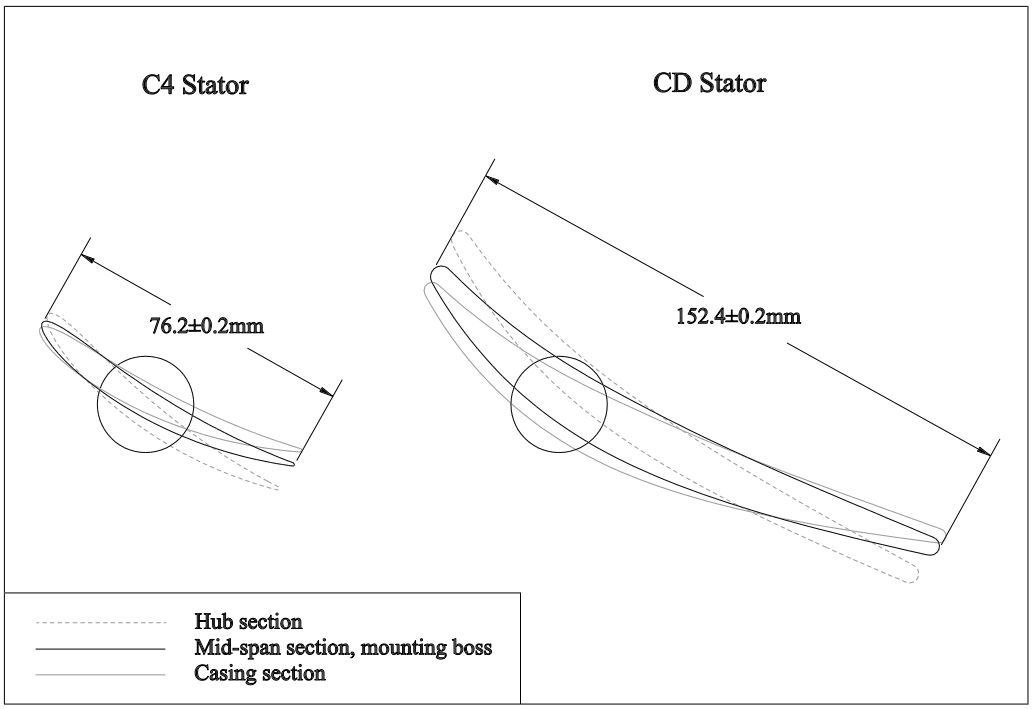

Figure 3.4: Radial view of C4 and CD stator blades showing hub, mid-span and tip sections.

The blades profiles were stacked about a radial axis to achieve free vortex flow at design load. The axial spacing between the rotor and CD stator blade rows was made similar to the existing SAG configuration with the C4 stator. This was achieved by locating the CD stator mounting boss a similar axial distance from the blade leading edge as in the C4 stator blade design. The resulting axial spacing, based on the CD stator chord length, was 18.4%c. The mounting boss positions for both stator blade rows are shown in Fig. 3.4.

A three-dimensional 'solid' model of the CD stator blade was developed using the commercial CADKey software. A series of spanwise profiles supplied by Hughes [84] were used to define the main blade surface. This surface was trimmed at hub and casing, allowing a nominal endwall clearance of 1.2 mm (0.5% of blade span).

The stator blades were manufactured by Complete Fabrication, Whittlesford, UK. Using the CAD model, a *master* blade was CNC machined from Prolab 65 modelling compound. For quality assurance, this blade was measured at 11 spanwise positions using a DEA global coordinate measuring machine with a reported accuracy of 1.5 μm. The maximum deviation from the design at mid-span was less than $\pm$0.2 mm around the leading edge ($\pm$6.9 percent of leading edge radius) and less than $\pm$0.3 mm over the whole section ($\pm$0.2 percent of chord).

A precision two-piece mould was taken from the master blade and used to mould the *production* blades for testing in the research compressor. All production blades were moulded out of fast setting epoxy resin filled with aluminium powder. A steel mounting boss was inserted into each blade during the moulding process. The bosses were machined out of mild-steel and featured a reinforcing shank which extended a distance of 100 mm into the blade surface. Each blade was lightly polished to achieve a smooth surface finish. For quality assurance, several profiles on a sample blade were measured using a laser scanning machine. The maximum deviation from the design was less than $\pm$0.4 mm on mid-span profile and $\pm$0.3 mm around the leading edge.

Several steps were required to replace the existing C4 stator blade row with the CD stator blade row. The compressor was opened at the shell piece housing the stator blade row. This allowed access to the rotor disk, which was slowly pushed off from the drive shaft by a hydraulic jack. The rotor disk was temporarily moved away from the compressor using a winch suspended from an overhead gantry. The shell piece containing the movable ring and stator blades was removed in the same way. A series of bolts in the inner ring were loosened, which removed the compressive force holding

the blade bosses into the inner ring sockets. Since the CD stator blade row contained exactly half the number of existing stator blade rows, stator blades were only fitted in every second socket. Plugs machined out of aluminium were used to fill the unused sockets so that the casing surface between stator blades remained uniform. The mid-span stagger angle was set using a jig referenced from the axial face of the inner ring. This allowed the blade stagger to be set with an estimated accuracy of $\pm 0.2^\circ$. All bolts were firmly tightened to lock the CD stator blades into the stator ring and the compressor was reassembled for testing.

3.4 Instrumentation

3.4.1 Pressure Measurement

Pressure measurements were made using two Datametrics Barocell pressure transducers. One transducer measured the absolute static pressure at inlet to the compressor (P_1) over a working range of $0-1000$ Torr. The other measured a differential pressure relative to P_1 over a working range of $0-100$ Torr. Each transducer was connected to a Datametrics signal conditioner where the gain was automatically selected by computer. Data sampling was automatically restarted if the gain setting reached the output limits of the signal conditioner or if the gain setting was adjusted during a measurement period.

The differential transducer was connected to a solenoid-actuated pneumatic switching valve (Scanivalve). This allowed up to 48 ports to be measured relative to the reference pressure P_1. The step and home signals for the Scanivalve valve were issued by computer.

Prior to commissioning of the turbulence grid (see Section 3.6), the reference pressure P_1 was measured by static tappings on the reference pitot-static tube at compressor inlet. Following installation of the grid, P_1 was measured by a ring tapping located on the outer wall of the inlet contraction. This was necessary for determining the inlet dynamic pressure using the method detailed in Appendix C.2. The difference in static pressure between these references was small and had negligible effect on calculation of air properties.

3.4.2 Relative Humidity Probe

The relative humidity was measured outside the wind tunnel using a Vaisala HUMICAP probe. The manufacturer specified accuracy of this instrument was $\pm 2\%$ relative humidity. Although the reference temperature and pressure were measured inside the wind tunnel at inlet to the compressor, any change in temperature across the inlet screen would be negligible.

3.4.3 Thermometer

The air temperature was measured at the compressor inlet using a Stow Laboratories platinum resistance thermometer. The manufacturer quotes an accuracy of $\pm 0.2^{\circ}$C for this instrument.

3.4.4 Multimeter

An Analogic DP100 5 (1/2) digital multimeter was used to measure AC anemometer bridge voltages during hot-wire measurements. The reported accuracy of AC readings was 0.45% of full scale output on the 200 mV range. The multimeter was computer controlled using an RS-232 interface.

3.4.5 Constant Temperature Anemometers

The hot-wire probe and hot-film sensors were controlled by two TSI–IFA100 intelligent flow analyzers. Both were TSI Model 158 Master Cabinets, containing individual TSI Model 150 anemometers with TSI Model 157 signal conditioners. Each unit could accommodate a maximum of 4 anemometers with signal conditioners; however these were divided between the cabinets with three installed in one cabinet and two installed in the other. The use of individual signal conditioners for each anemometer allowed the bridge voltages to be amplified and low-pass filtered prior to data acquisition. A subroutine written in Labview optimised the gain and offset settings of the signal conditioners to achieve the greatest signal range for the data acquisition card. A maximum of five anemometers could be operated simultaneously.

3.4.6 Hot-Wire Probes

Single-element hot-wire probes were used for making fast-response velocity measurements in the research compressor. The probes were controlled by a TSI–IFA150 anemometer described in Section 3.4.5. The probe calibration was based on an experimental study by Collis and Williams [23], in which the heat transfer rate from heated wires was measured in low Reynolds number flows. The research showed that Nusselt number could be accurately related to Reynolds number over a range of Reynolds numbers (0.01–140) and they proposed a functional relationship to describe their observations. A discontinuity in the experimental measurements was observed at a Reynolds number of 44. This was attributed to the development of eddy shedding associated with the formation of a Karman vortex street. This flow phenomenon also had the effect of changing the empirical constants used in the relationship. Fortunately, the range of Reynolds numbers experienced by small diameter hot-wire elements in low-speed flows is considerably less than this eddy shedding frequency. The relationship also became inaccurate in very low Reynolds number flows where natural convection

effects can significantly influence heat transfer rates.

The functional relationship proposed by Collis and Williams [23] was later modified by Walker [175] to improve correlation with experimental calibration data. This was achieved by including a quadratic term. The modified expression may be written as

$$Nu\left(\frac{T_m}{T_a}\right)^{-0.17} = a\left(Re_d^{0.45}\right)^2 + b\left(Re_d^{0.45}\right) + c \tag{3.2}$$

where T_m is the mean temperature between the wire (T_w) and free-stream air (T_a), $Re_d = \rho U d/\mu$ is the Reynolds number for wire diameter d, and the constants a, b and c are determined by experimental calibration. The Nusselt number may be expressed as

$$Nu = \frac{Q}{\pi L(T_m - T_a)k_a} \tag{3.3}$$

$$= \frac{E^2 R_p}{\pi L(T_m - T_a)k_a\left(R_t\right)^2} \tag{3.4}$$

where Q is the heat transfer rate from the wire, E is the anemometer bridge voltage, R_p is probe operating resistance, L is the element length, k_a is the thermal conductivity of air and R_t is the combined resistances of the probe, cables and series resistor used in the anemometer bridge. The fluid properties k_a and μ were evaluated at the mean film temperature T_m.

The temperature of the probe element was controlled by selection of an appropriate operating resistance. All measurements in the present study used a fixed overheat ratio of 1.6 (the ratio of operating resistance to cold resistance). This operating resistance was estimated to give a wire temperature of approximately $T_w = 180°\mathrm{C}$.

The hot-wire probe was calibrated inside the research compressor using an in-situ method developed by Solomon [154]. In this method, a local velocity was measured using a three-hole probe over a range of flow speeds. Following this, the three-hole probe was removed from the compressor and the process was repeated using the hot-wire probe. These results were used to determine the empirical constants of the calibration equation Eq. (3.2). Solomon [154] also performed probe calibrations in a closed loop wind tunnel. However, the benefits of the controlled wind tunnel environment were outweighed by large errors introduced by changing contact resistances which occurred during disassembly and reassembly of the probe in the wind tunnel. Solomon [154]

measured errors of the order of 10% velocity. The in-situ method eliminated this problem and provided a simple and fast way of checking the probe calibration before and after each test.

In-situ calibrations were performed before and after each traverse measurement to ensure large changes in calibration had not occurred. Slow calibration drifts are common during traverse measurements due to accretion of small particles on the wire. Several measurement points were remeasured after completion of the traverse. The drift measured at these points was correlated against time elapsed. The linear regression of the dataset was constrained so that zero drift occurred at the start of the traverse (time = 0). A correction was applied to each measurement point based on the time elapsed. The accuracy of velocity measurements, taking into account the accuracy of the three-hole probe, was estimated to be better than $\pm 1\%$ of a reading.

3.4.7 High-Speed Data Acquisition

The data acquisition for hot-film and hot-wire measurements was effected with an United Electronic Industries Win30DS card. This card featured simultaneous sampling of 16 analogue input channels with a 12-bit analogue-to-digital resolution. The maximum sampling rate across all channels was 750 kHz. The sampling process could be initiated by computer or through an external trigger. The trigger function of the card was initialised by setting a digital output on the BNC interface card. The maximum time for aperture matching across all 16 channels was 15 ns or 0.001% of a rotor passing period at maximum speed. The input range of the card was software selectable as either a bipolar range of -5 to $+5$ volts or unipolar range of 0 to $+5$ volts.

The high-speed data acquisition process involved taking repeated measurements, each from separate rotor revolutions triggered at the same rotor phase. Two methods of triggering were available for use during testing. The first method used a timing pulse issued from the Baldwin Precision shaft encoder connected to the motor drive shaft. The pulse was issued at a rotor phase determined by Solomon [154] to have a high level of periodicity in rotor wakes. The second method of triggering was introduced by Hughes [83] to assess the amount of twist in the rotor shaft that results from changing torsional load on the drive shaft and couplings. This was an optical-reflective device (IRD Mechanalysis 21000c) which produced an electrical pulse when light was reflected from a small target back into the sensor. The device was mounted on the outside of

the wind tunnel adjacent to the rotor blade row. A small hole was drilled through the casing and sealed with a perspex plug to provide direct line of sight to the rotor blade row. A small reflective target was attached to the end of a rotor blade. This rotor blade was chosen to give a similar triggering position as the pulse emitted from the shaft encoder. Hughes [83] found the amount of twist remained constant at a fixed speed setting but varied with the load on the shaft. The standard deviation of the difference between the timing signals for a fixed speed and load was estimated to be less than 0.8% of a blade passing period. As a result, both methods of triggering were considered suitable for the triggering of data acquisition.

3.4.8 Three-Hole Probe

A three-hole probe was calibrated to measure the flow angle, total pressure and dynamic pressure. The probe was an United Sensor two-dimensional cobra probe, type CA120 with 3.175 mm (1/8 inch) diameter sensing head. The tubes numbers were stamped into the reference bar located at the opposite end of the probe. The tubes order is 2,1,3 when viewed from top to bottom as shown in Fig. 3.5.

Figure 3.5: United Sensor CA120 three-hole probe

Solomon [154] developed a functional basis for calibrating the probe by considering the ideal flow around a cylinder. Three functions were defined in terms of flow angle (α), probe geometry and Reynolds number. These are given by

$$f_1(\alpha, \text{geometry}, Re) = \frac{p_2 - p_3}{p_1 - p_3} \tag{3.5}$$

$$f_2(\alpha, \text{geometry}, Re) = \frac{p_1 - p_3}{\frac{1}{2}\rho U^2} \tag{3.6}$$

$$f_3(\alpha, \text{geometry}, Re) = \frac{P - p_1}{\frac{1}{2}\rho U^2} \tag{3.7}$$

where P is total pressure and U is the local velocity upstream from the probe. Given a fixed probe geometry, the three functions were calibrated over a range of flow angles and Reynolds numbers. The flow angle may be directly obtained from Eq. (3.5). Coefficients of dynamic and total pressure may be determined from

$$Cp_{dyn} = \frac{(p_1 - p_3)}{f_2(\alpha)(P_{in} - p_{in})} = \frac{(p_1 - p_3)}{f_2(\alpha)\left(\frac{1}{2}\rho V_a^2\right)} = \left(\frac{U}{V_a}\right)^2 \tag{3.8}$$

$$Cp_{tot} = \frac{f_3(\alpha)(\frac{1}{2}\rho U^2) + (p_1 - p_{in})}{(P_{in} - p_{in})} = \frac{P - p_{in}}{\frac{1}{2}\rho V_a^2} \tag{3.9}$$

The probe calibration was initially repeated in the present study using a calibration nozzle. However, the results showed large discrepancies from the previous calibration by Solomon [154]. This was thought to be caused by a spurious immersion effect or a static pressure gradient in the jet. The calibration was repeated in a large closed-loop wind tunnel at a flow speed of 20 m/s. Figure 3.6 shows these results to agree well with the previous calibration results from Solomon [154]. Solomon [154] calibrated the probe over the range of flow speeds that were likely to be encountered during testing in the research compressor. The results show little dependence on flow speed and as a consequence no correction for Reynolds number was applied. The calibration functions used in this thesis are shown in Fig. 3.6.

The probe was attached to a support that allowed traversing in both radial and axial directions. The uncertainty in probe alignment was estimated to be approximately ± 0.5 mm. The probe support allowed yaw angle adjustment with position shown on a vernier scale with 0.1° intervals. A horizontal reference angle was defined by placing a spirit level on the probe reference bar and adjusting the probe support until a horizontal reading was achieved. The accuracy in setting the probe angle was estimated to be better than $\pm 0.2^\circ$.

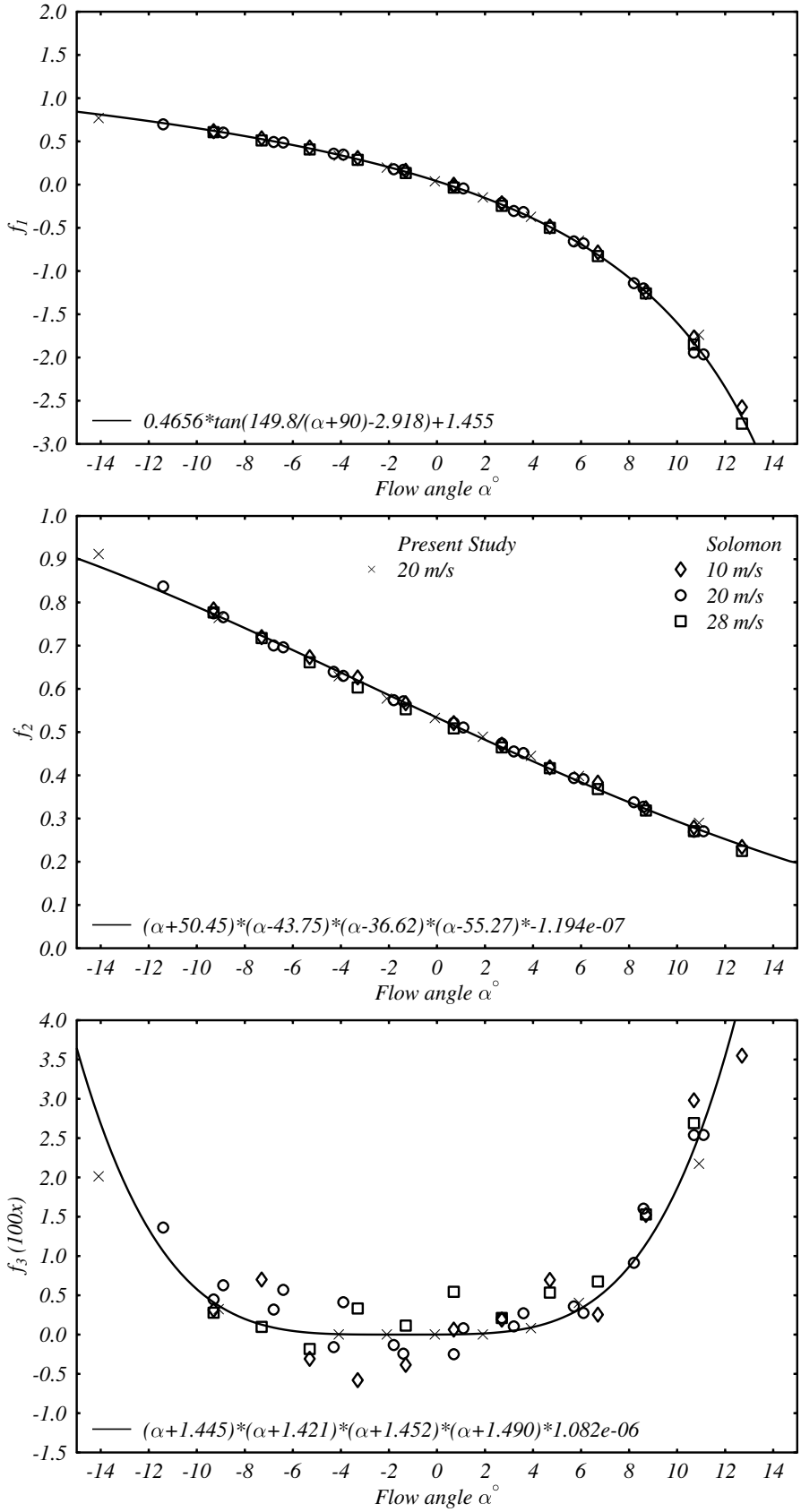

Figure 3.6: United Sensor CA120 three-hole probe calibration

3.5 Research Compressor Control

The research compressor was controlled using a two computer arrangement. All low level control functions and low-speed data acquisition were performed by a computer running an object orientated TurboPASCAL program written by Solomon [154]. This computer was instrumented with a Metrabyte DAS-20 card, two relay cards and a serial communication card. The computer performed several functions: range control of the pressure transducer signal conditioners, acquisition of pressure transducer data, control of the Scanivalve pressure switching valve, control of both IGV and stator blade row stepper drives and acquisition of temperature and relative humidity data. The computer also calculated and controlled the the compressor flow coefficient ($\phi = V_a/U_{mb}$) by adjusting the throttle opening. The compressor speed could be maintained at constant set points of Mach number, reference Reynolds number or rotor speed. The program also controlled a RS-232 interface, which allowed commands and data to be exchanged with other computers and devices. A second computer was used for high-speed data acquisition and issuing high level control commands.

3.5.1 Speed Control

The 30 kW DC motor was controlled by a non-regenerative Natronics Stardrive unit. An analogue control circuit continuously adjusted the motor speed to match the speed feedback voltage to an external demand voltage. The feedback voltage was generated by an in-house frequency-to-voltage converter connected to a Baldwin Precision shaft encoder directly coupled to the motor shaft. The encoder issued 6000 pulses per revolution. The in-house frequency to voltage converter also communicated the speed to computer using a four digit binary coded decimal (the least significant digit was 0.1 rpm). The computer issued a demand voltage using the digital-to-analogue function of the Metrabyte DAS-20 card. This allowed accurate control of the research compressor speed. The computer control could also be bypassed by a manual speed control.

The stability of the machine speed varied somewhat over the range of test speeds, but was generally better than ± 0.2 rpm at fixed speed settings used for detailed measurements.

3.5.2 Flow Coefficient

Prior to installation of the turbulence grid, a pitot-static tube was used to measure the dynamic pressure at compressor inlet ($0.5\rho V_a^2$). The total pressure tapping on the nose of the tube was located 175.1 mm axially upstream from the IGV blade row at a radial distance of 127.6 mm from the hub wall. The pitot-static tube was manufactured by Airflow Developments and featured an ellipsoidal nose with an external diameter of 4 mm. The static tappings of the tube were 30 mm from the leading edge. The inlet velocity V_a was determined from the measured dynamic pressure and air properties and was used to calculate the flow coefficient $\phi = V_a/U_{mb}$.

The velocity distribution was measured across the annulus by inserting the reference pitot-static tube at different radial positions. The total pressure tapping was positioned 175.1 mm axially upstream from the leading edge of the IGV blade row. Measurements were made at a constant reference Reynolds number $Re_c = 120000$ at several flow coefficients ($\phi = V_a/U_{mb}$): 0.600, 0.675 and 0.840. The velocity was found to vary by no more than 2.0% from radial average value, excluding readings in the endwall boundary layers. The velocity measured at the normal reference position of the pitot-static tube was found to differ by no more than 1.6% of the radial average value.

Solomon [154] examined the stability of the dynamic pressure at a fixed compressor operating point ($Re_c = 120000$, $\phi = 0.7$). Measurements of the dynamic pressure showed a recurring fluctuation over a period of approximately 30 seconds. This was thought to be caused by either large scale eddies in the laboratory or a Kelvin–Helmholtz type of resonance in the diffuser.

An alternative method of determining flow coefficient was required for use with the turbulence grid, since the grid would have influenced readings from the reference pitot-static tube located shortly downstream. A short computational study of the inlet contraction was used to determine suitable locations for new reference tappings (see Appendix C.1). Static ring tappings were placed on the core and shell of the inlet contraction and then were calibrated against the reference pitot-static tube prior to installation of the grid (see Appendix C.2).

3.6 Turbulence Generating Grid

A turbulence grid was installed in the research compressor inlet to make the flow more representative of an embedded row in a multi-stage machine. The final design, shown in Fig. 3.7, consisted of 38 brass rods of 7.84 mm diameter. The rods were orientated radially and were attached at each end to a thin brass strip fastened to the tunnel walls. The grid was installed immediately after the inlet contraction with the intention of providing sufficient streamwise distance for the rod wakes to mix-out before reaching the compressor section.

The turbulence grid added further resistance to the flow through the research compressor, thus lowering the maximum achievable flow coefficient. However, this restriction was sufficiently small to allow compressor operation over the required range of test cases. The design of the turbulence grid is detailed in Appendix B.

Figure 3.7: Photograph of the research compressor inlet section showing the turbulence grid